



Hot tensile deformation behavior and microstructural evolution of a Mg–9.3Li–1.79Al–1.61Zn alloy

Furong Cao ^{a,*}, Fei Xia ^{a,b}, Guoqiang Xue ^a

^a School of Materials and Metallurgy, Northeastern University, Shenyang 110819, PR China

^b Suzhou Suxin Special Steel Co., Ltd., Suzhou 215151, PR China

ARTICLE INFO

Article history:

Received 2 October 2015

Received in revised form 28 October 2015

Accepted 5 December 2015

Available online 8 December 2015

Keywords:

Mg–Li–Al–Zn alloy

Hot tensile deformation

Microstructure

Constitutive equation

Dynamic recrystallization kinetics

ABSTRACT

To explore the nature of hot plastic deformation, the microstructures and hot tensile deformation modeling in a rolled Mg–9.3Li–1.79Al–1.61Zn alloy were investigated. Microstructural study reveals that at the temperatures of 473 and 523 K with strain rates of less than $1.67 \times 10^{-4} \text{ s}^{-1}$, partial dynamic recrystallization (DRX) or continuous DRX takes place, whereas at the temperatures of 573 and 623 K at most strain rates, complete DRX and pronounced dynamic grain growth occur. The maximum superplasticity of 566.7% was demonstrated in the present alloy at the temperature of 573 K and the strain rate of $1.67 \times 10^{-4} \text{ s}^{-1}$. A constitutive equation was established by regression analysis of Arrhenius type hyperbolic sine function and the activation energy for deformation of the present alloy was calculated as 141.12 kJ/mol. The critical parameters at the characteristic points of flow stress curves were determined and the relationship between DRX volume fraction and strain was established by Avrami type equation. Finally, the relationship between dislocation density and Zener–Hollomon parameter was modeled and the conditions of critical peak dislocation density and critical peak stress for the initiation of DRX were derived. The theoretical prediction is consistent with the experimental result.

© 2015 Elsevier Ltd. All rights reserved.

1. Introduction

Mg–Li alloys are the lightest non-toxic metallic material up to date. Due to their high specific strength, high specific stiffness, excellent damping capabilities, and good electromagnetic shielding properties, they have the potential for use in areas such as spaceflight, weapons, 3C products, and automobile manufacturing. For this reason, recently, Mg–Li alloys have attracted extensive interests of researchers and are becoming a hot topic [1–7]. Generally speaking, magnesium has poor deformability at room temperature because of its hexagonal closed packed (HCP) crystal structure and limited slip systems. The addition of Li with a body-center cubic (BCC) structure to Mg will improve the deformability and raise the ductility. However, because binary Mg–Li alloys have low strength, it is necessary to add the third or the fourth strengthening elements. Al and Zn elements are good candidates for reinforcing the matrix of Mg–Li binary alloy. Thus, a new Mg–9.3Li–1.79Al–1.61Zn (designated as LAZ922) alloy was designed. However, little information is available reporting the detailed microstructural evolution during hot tensile deformation in LAZ922 alloy. In order to explore its capability of plasticity and microstructural evolution at elevated temperatures, it is necessary to investigate its hot tensile deformation behavior and microstructures.

Constitutive modeling and dynamic recrystallization (DRX) kinetics are one of the most important topics during hot deformation. Constitutive equation describes the dependence of flow stress on the deformation temperature and the strain rate etc. and is widely used in mechanics simulation and industrial circle. DRX kinetics describes the relationship between DRX volume fraction and strain, i.e., Avrami type equation, and helps deepen the understanding of the DRX evolution mechanism. In recent years, some works on DRX behavior have been reported over a wide range of materials such as steels [8,9], Ni-based alloy [10], Ti-based alloys [11,12], CuZn40Pb2 alloy [13], and (Mg–Zn–Zr and Mg–Al–Zn) Mg alloys [14,15] for hot compression deformation. Limited research works have been recorded for hot tensile deformation [16,17] and hot torsion [18,19]. To the best of our knowledge, except the work on hot compression behavior in as-cast LA93–1.0Nd alloy [20], little work is available reporting the constitutive equation and the DRX kinetics during hot tensile deformation in as-rolled LAZ922 alloy, linking the dislocation density to Zener–Hollomon (Z) parameter, and deriving the critical conditions of peak dislocation density and peak stress. It is necessary, therefore, to investigate the constitutive modeling, the DRX kinetics etc. of LAZ922 alloy via uniaxial tensile deformation at elevated temperatures.

In this work, our aim is threefold. First, the microstructures and mechanical properties of a novel LAZ922 alloy fabricated by casting and rolling are investigated. Second, a hyperbolic sine Arrhenius type constitutive equation and the DRX kinetics based on Avrami type equation are established based on the flow stress curves. Third, the relationship

* Corresponding author.

E-mail addresses: cfr-lff@163.com, caofr@smm.neu.edu.cn (F. Cao).

between dislocation density and Zener–Holloman parameter and the conditions of critical peak dislocation density and critical peak stress for the initiation of DRX are investigated.

2. Experimental procedures

2.1. Material preparation and tensile testing

Detailed casting and rolling process of LAZ922 alloy was shown elsewhere [7]. The chemical composition was 9.3 mass% Li, 1.79 mass% Al, 1.61 mass% Zn, and balanced Mg. Dog bone samples whose tensile direction was parallel to the rolling direction were punched on the stamping machine. The dimensions of the dog bone sample were 1.8 mm in thickness, 10 mm in gauge length, and 6 mm in gauge width. Prior to tensile deformation, the stamped samples passed annealing treatment at 553 K for 1 h. Tensile deformation was carried out on Model CMT5105 microcomputer controlled universal electronic tensile machine equipped with a heating chamber at temperatures of 473–623 K over initial strain rates of 1.67×10^{-4} – $1.67 \times 10^{-2} \text{ s}^{-1}$. The holding time prior to tensile deformation was 15 min. After elongated to failure, the samples were quenched into cold water to reserve the deformed microstructures. Then the quenched samples were dried by an electric blower and sealed in a safety place to avoid the reaction and oxidation.

2.2. Microstructure examination

The samples for optical microscope (OM) observation were ground, polished, and etched in the solution of 10% HCl + 90% ethanol. The etched samples were rinsed in alcohol, dried, and placed in a dry vessel. The micrographs of the prepared samples were taken on an Olympus DSX500 optical microscope. Phase volume fraction and grain size were measured by Image Pro Plus software and the grain size was equivalent to the linear intercept grain size (d).

The samples for transmission electron microscope (TEM) investigation were ground to about 50 μm by carborundum paper. The disks in 3 mm diameter were punched by press, and were acid-jetted in the 10% HClO_4 + 90% ethanol electrolyte at temperatures ranging from 238 to 243 K. TEM observations were conducted on Tecnai G^{20} transmission electron microscope.

The samples for X-ray diffraction (XRD) analysis were polished to ensure the flatness of their surfaces. The polished samples were observed on X'Pert Pro X-ray diffractometer.

3. Results

3.1. Microstructures

3.1.1. Initial microstructure before high temperature deformation

Fig. 1 shows the initial microstructure and its TEM images and XRD pattern before high temperature deformation. In Fig. 1(a), the as-annealed initial microstructure mostly consists of elongated grains. The white phase is HCP-structured α -Mg phase and the yellow phase is BCC-structured β -Li phase. Black particles precipitate out and disperse in the β -Li phase. It is found in Fig. 1(b) that numerous short-bar-like phases exist inside the β -Li grain and take on a certain crystal orientation and found in Fig. 1(c) that such a phase also exists at the triple grain boundaries. To ascertain the precipitates in Fig. 1(b) and (c), selected area diffraction (SAD) analysis was carried out. The SAD patterns are shown in Fig. 1(e) and (f). The incidence zone axes of diffraction spots for the second phase in Fig. 1(e) and (f) are $[111, 110]$, respectively. The short-bar-like precipitates were determined as AlLi phase, a cubic (NaTl) structure, as shown by the crystal indexes. XRD analysis of Fig. 1(d) confirms that this phase is AlLi phase. Thus, the black particles in Fig. 1(a) are AlLi phase. XRD results reveal that Zn element probably dissolves into the matrix of the present alloy. Similar

to the Mg–10Li–1Al alloy which is composed of α , β , and AlLi phases based on Mg–Li–Al phase diagram [21], as-annealed LAZ922 alloy also consists of the same phase composition and the difference is that Zn element dissolves in the matrix. The reason is that because of bigger difference in the electronegativity of Al (1.61) and Li (0.98) [22], the AlLi phase has a stronger binding energy and hence is stable in the as-annealed state. Therefore, the initial microstructure consists of α -Mg, β -Li, and AlLi phases.

3.1.2. Microstructures at different deformation temperatures

3.1.2.1. OM microstructures at the deformation temperatures of 473 and 523 K. Fig. 2 shows the microstructures of LAZ922 alloy at the deformation temperature of 473 K with different strain rates. The white phase is α -Mg phase and the black or gray phase is β -Li phase. The elongated grains parallel to the horizontal longitudinal rolling direction still exist after the alloy undergoes deformation, indicating that DRX does not fully complete or partially completes. This is because the elongated grain microstructure is a non-DRX microstructure with predominant low angle grain boundaries and the equiaxed grain microstructure is a complete DRX microstructure with predominant high angle grain boundaries. The microstructures in Fig. 2 consist of elongated grains and equiaxed grains and are mixed microstructures. Thus, DRX does not fully complete or partially completes in Fig. 2. In Fig. 2(a), grain morphology basically does not change. However, in Fig. 2(b) and (c), obvious in-situ DRX or partial DRX takes place. Numerous small grains fragment and form in the big elongated grains. This characteristic shows that continuous DRX takes place. In Fig. 2(d), numerous isolated equiaxed grains form but the trace of elongated grain is still visible. With the decrease of strain rate, partial DRX progresses, the number of fine grains increases and the grain size becomes smaller. Thus, grains are refined due to partial DRX as compared with the initial microstructure in Fig. 1(a).

Fig. 3 shows the microstructures of LAZ922 alloy at the deformation temperature of 523 K with different strain rates. In Fig. 3(a), (b) and (c), elongated grain still exists after tensile deformation at the strain rates of 1.67×10^{-2} , 1.67×10^{-3} , and $5 \times 10^{-4} \text{ s}^{-1}$, which indicates that partial DRX takes place. However, in Fig. 3(d), elongated grains disappear and equiaxed grains form in random crystal orientation due to grain rotation under applied stress, indicating that complete DRX occurs at the strain rate of $1.67 \times 10^{-4} \text{ s}^{-1}$. Grain size decreases and elongation to failure increases with decreasing the strain rates from 1.67×10^{-2} to $1.67 \times 10^{-4} \text{ s}^{-1}$. Moreover, grains are further refined as compared with the microstructures in Fig. 2.

Table 1 shows the measured and theoretically determined volume fractions of α and β phases of LAZ922 alloy at 473–523 K. First, the measured phase volume fractions show that β phase volume fraction (V_β) does not take on regular variation, indicating that variation in phase ratio is closely related to local microstructural inhomogeneity. Second, the mean phase volume fractions reveal that β phase volume fraction at 523 K is greater than that at 473 K, and β phase volume fraction in Fig. 2(d) is larger than that in Fig. 2(c), indicating that the β phase volume fraction increases as the temperature increases and the strain rate decreases, contrary to the experimental results of superplastic Mg–8.5Li alloy at 573 and 623 K in Ma et al. [23] that β phase volume fraction decreases due to Li loss. Third, the theoretical volume fractions of β phase determined by lever rule [24] are obviously larger than the measured and mean volume fractions of β phase, indicating that Li loss occurs under experimental condition. These three findings indicate that the phase ratio variation in LAZ922 alloy is complicated, is relevant to the microstructural inhomogeneity, and even is closely related to the processing history because the cast and rolled microstructural inhomogeneities inherit into the hot deformation microstructures. Further study on this issue is required in the future.

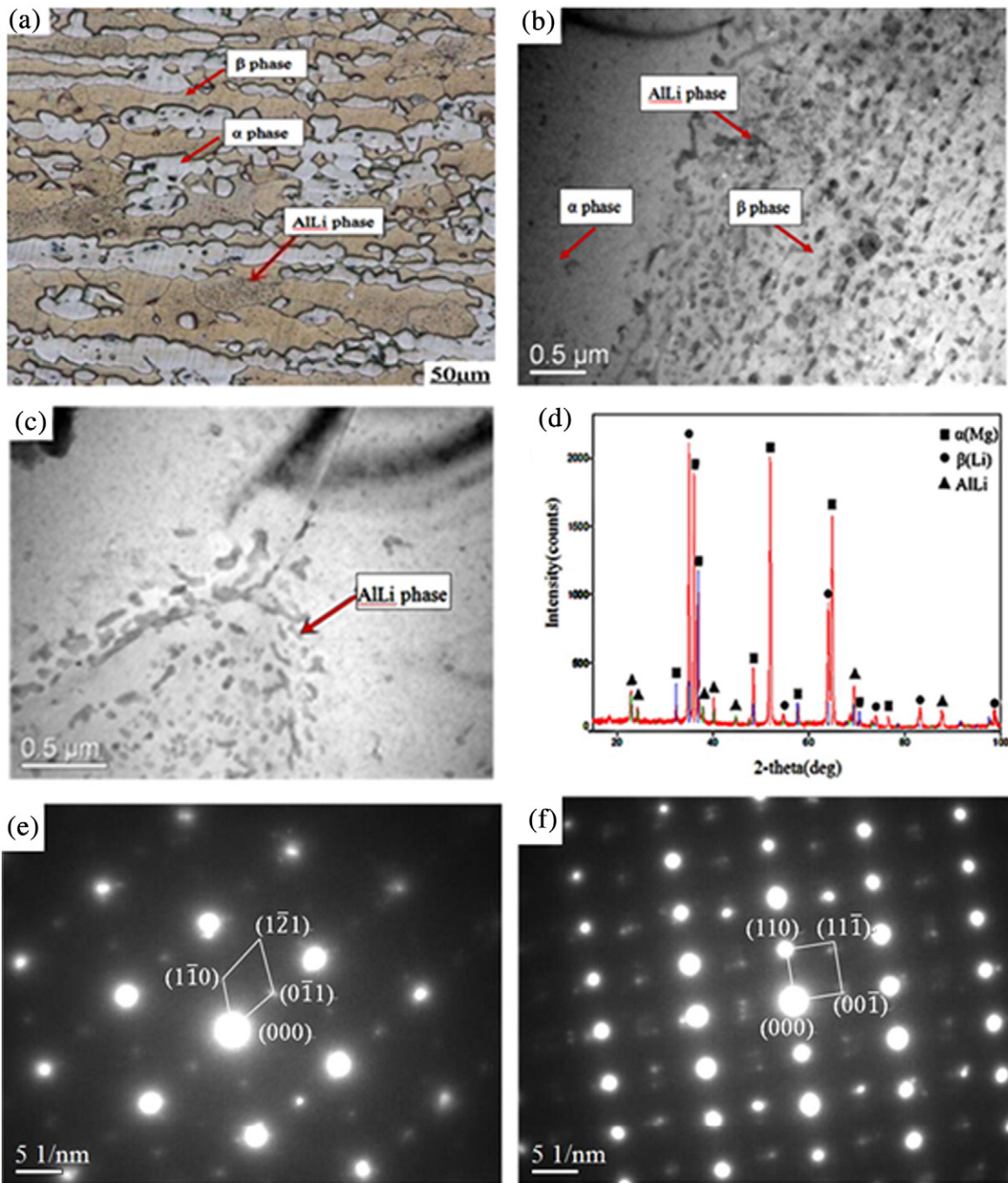


Fig. 1. Initial microstructure and its TEM images and XRD pattern before high temperature deformation. (a) Initial OM annealed microstructure, (b) TEM AlLi phase inside β -Li grain, (c) TEM AlLi phase at triple grain boundaries, (d) XRD pattern, (e) SAD pattern with the zone axis [111], and (f) SAD pattern with the zone axis [110].

3.1.2.2. OM microstructures at the deformation temperatures of 573 and 623 K. Fig. 4 shows the microstructures of LAZ922 alloy at the deformation temperature of 573 K with different strain rates. In Fig. 4(a), a few big (elongated) grains coexist with numerous small equiaxed grains. Big grain size reaches 50 μm while small grain size reaches several micrometers, which indicates that this microstructure is not homogeneous. From Fig. 4(b) to (c) and (d), complete DRX takes place and equiaxed grains form. The grain microstructures are homogeneous as comparison with Fig. 4(a). From Fig. 4(b) to (c) and (d), pronounced dynamic grain growth occurs, and the grain sizes and the elongations to failure increase with decreasing the strain rates. In Fig. 4(d), the present alloy exhibits maximum superplasticity of 566.7% at the temperature of

573 K and the strain rate of $1.67 \times 10^{-4} \text{ s}^{-1}$ with a grain size of 33.38 μm .

Fig. 5 shows the microstructures of LAZ922 alloy at the deformation temperature of 623 K with different strain rates. As shown in Fig. 5(a), the grain size (14.22 μm) is greater than that (13.28 μm) in Fig. 4(a) and a few elongated grains distribute in the matrix, indicating that the microstructure still is not homogeneous. In Fig. 5(b) and (c), the grain sizes at 623 K at 1.67×10^{-3} and $5 \times 10^{-4} \text{ s}^{-1}$ reach 20.67 and 34.36 μm , respectively, which exceed the grain sizes at 573 K at the same strain rates. These results show that grain growth at 623 K is more pronounced than that at 573 K. The lower the strain rate, the bigger the grain size. Also, the number of equiaxed grains increases with

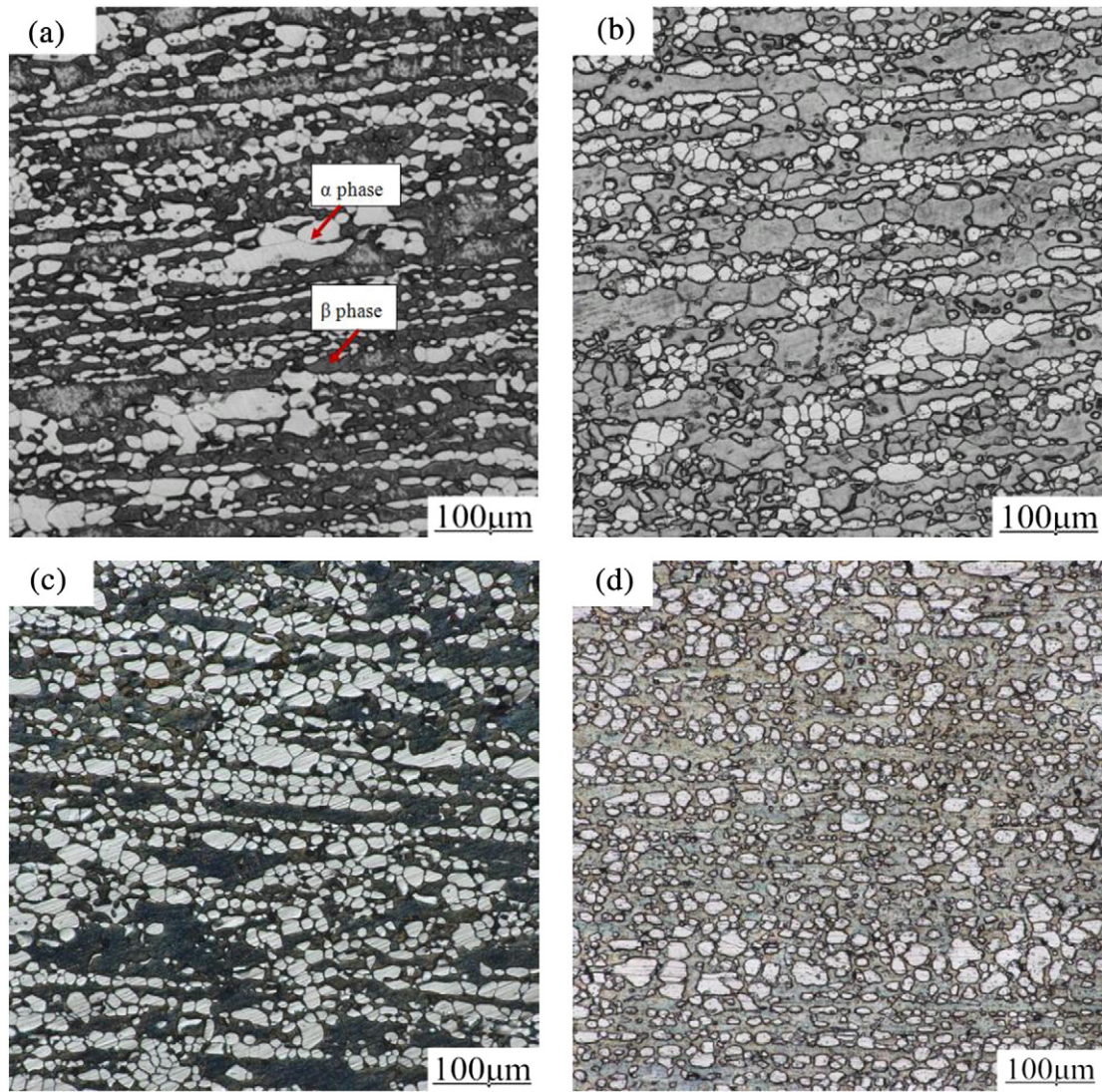


Fig. 2. Microstructures of LAZ922 alloy at the deformation temperature of 473 K with different strain rates and grain sizes/elongations to failure. (a) $1.67 \times 10^{-2} \text{ s}^{-1}$, 16.92 μm /28.6%, (b) $1.67 \times 10^{-3} \text{ s}^{-1}$, 15.08 μm /37.5%, (c) $5 \times 10^{-4} \text{ s}^{-1}$, 14.89 μm /37.5%, and (d) $1.67 \times 10^{-4} \text{ s}^{-1}$, 12.80 μm /55.6%.

decreasing the strain rate, revealing that the microstructures are composed of high angle grain boundaries and complete DRX has been accomplished prior to the grain growth.

In consideration of the results obtained from Figs. 2–5, we can conclude that at the same temperature, the lower the strain rate, the more complete the DRX, and the more the number of equiaxed grains. The reason is that for deformation at lower strain rate, there is enough time to induce the occurrence of DRX. At the same strain rate, the higher the temperature, the more complete the DRX. The reason is that high temperature accelerates atomic diffusion, annihilates the dislocations, and promotes the occurrence of DRX. At higher temperatures, complete DRX followed by significant grain growth takes place and the grain shapes become more equiaxed.

3.2. Flow stress curves

Fig. 6 shows the true stress–true strain curves (flow stress curves) of LAZ922 alloy at different temperatures at different strain rates. Deformation temperature and strain rate have a remarkable effect on the flow stress curves. The stress level decreases with increasing the deformation temperature and/or decreasing the strain rate. The flow stress curves exhibit three distinct stages. At the initial stage of tensile deformation, strain hardening or work hardening predominates and the

flow stress increases sharply up to the critical stress with increasing strain. In this case, dislocation multiplication appears and dislocation density increases. At the second stage, i.e., straining from the critical stress to the peak stress, the formation of new grains leads to a gradual decrease in the work hardening rate. When the hardening rate becomes equal to the softening rate, the peak stress is reached. At the third stage, the flow softening exceeds the hardening and the stress decreases. A steady-state flow is exhibited in individual curves.

The flow stress change is complicated at the third stage. Some of the flow curves only have a softening stage but do not have steady-state stage, whereas the other curves exhibit a hardening stage, indicating that the flow curves of hot tensile deformation exhibit their unique characteristics. In Fig. 6(a), (b) and (c), the flow stress curves at 473 and 523 K with strain rates of 1.67×10^{-2} – $5 \times 10^{-4} \text{ s}^{-1}$ exhibit a rapid decrease beyond the peak stress and do not have a steady-state plateau, which corresponds to the microstructures of incomplete DRX or partial DRX shown in Figs. 2 and 3; the flow stress curves at 573 and 623 K with strain rates of 1.67×10^{-2} – $5 \times 10^{-4} \text{ s}^{-1}$ exhibit a gradual decrease beyond the peak stress and exhibit the flow softening characteristic. In Fig. 6(c), the flow stress curve at 573 K and $5 \times 10^{-4} \text{ s}^{-1}$ exhibits typical DRX characteristics and beyond the peak stress, the stress gradually decreases and reaches a steady-state plateau, i.e., a dynamic balance between the dynamic softening and the working

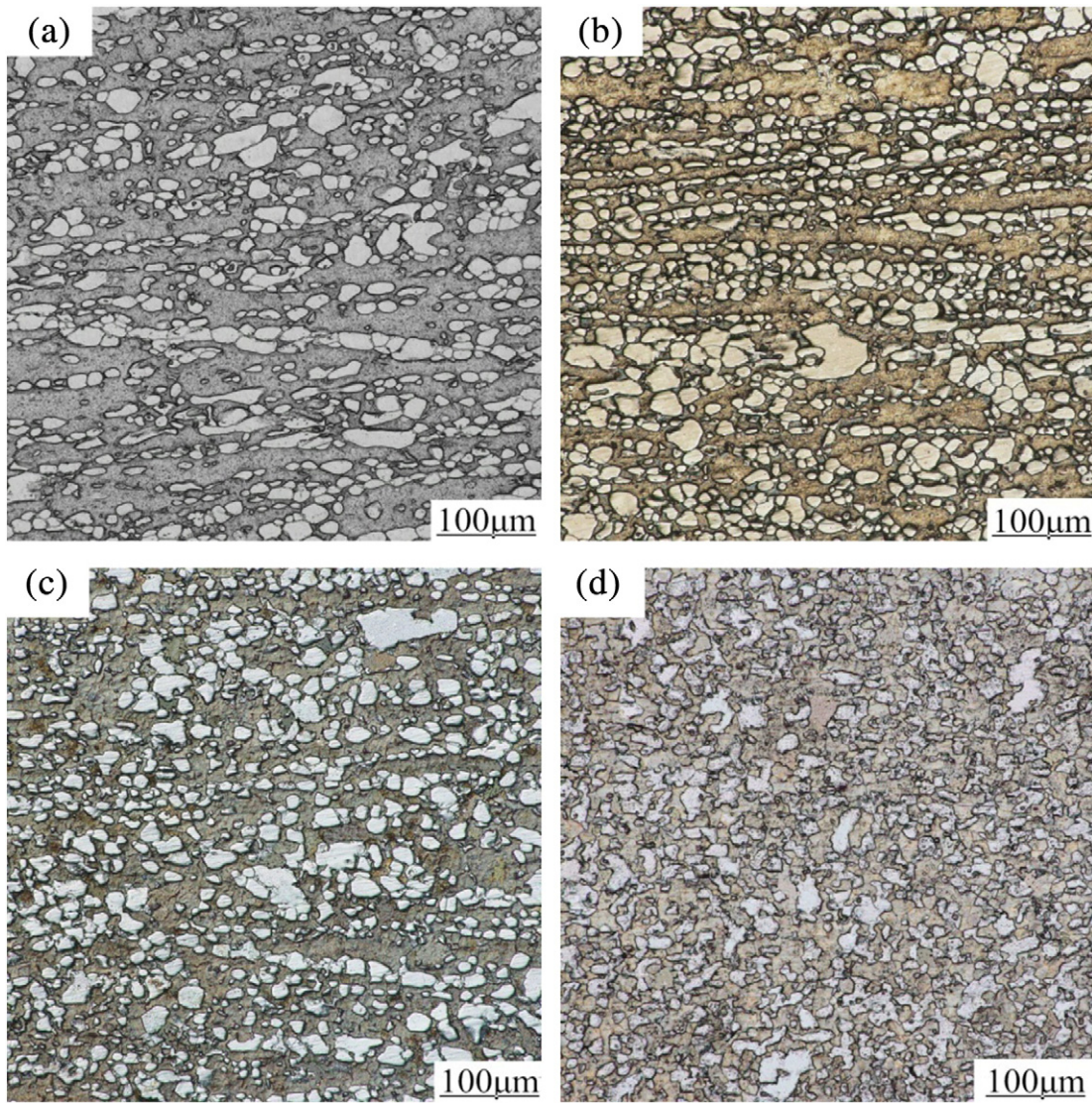


Fig. 3. Microstructures of LAZ922 alloy at the deformation temperature of 523 K with different strain rates and grain sizes/elongations to failure. (a) $1.67 \times 10^{-2} \text{ s}^{-1}$, 15.85 μm /71.4%, (b) $1.67 \times 10^{-3} \text{ s}^{-1}$, 14.96 μm /62.5%, (c) $5 \times 10^{-4} \text{ s}^{-1}$, 13.82 μm /112.5%, and (d) $1.67 \times 10^{-4} \text{ s}^{-1}$, 12.51 μm /177.8%.

hardening. However, in Fig. 6(c) and (d), the flow stress curves at 623 K and $5 \times 10^{-4} \text{ s}^{-1}$ and at 573 K and $1.67 \times 10^{-4} \text{ s}^{-1}$ exhibit a peculiar hardening with increasing strain, which corresponds to the dynamic grain growth in Figs. 5(c) and 4(d). The causes of flow softening and peculiar hardening phenomena at the third stage in LAZ922 alloy will be discussed in Section 4.1.2.

Fig. 7 shows the relationship of logarithm stress as a function of logarithm strain rate at the true strain of 0.2, through which strain rate sensitivity exponents or m values ($m = \text{dln}\sigma / \text{dln}\dot{\epsilon}$) are represented by the triangle. At 573 K, m value increases with decreasing the strain rate. The m value at 573 K and $1.67 \times 10^{-4} \text{ s}^{-1}$ corresponding to 566.7%

elongation is 0.527, revealing that grain boundary sliding (GBS) may take place. Big elongation to failure in superplasticity usually corresponds to high m value, whereas high m value does not mean that it must have big elongation to failure, e.g., the specimen with the m value of 0.645 at 473 K and $1.67 \times 10^{-4} \text{ s}^{-1}$, only 55.6% elongation to failure is exhibited.

3.3. Constitutive equation

The constitutive equation can be described by Arrhenius type hyperbolic sine law for a wide range of stresses [25–28]:

$$\dot{\epsilon} = A [\sinh(\alpha\sigma)]^n \exp(-Q/RT) \quad (1)$$

where $\dot{\epsilon}$ is the strain rate, A is a dimensionless constant, α is the material constant, σ is the flow stress, here peak stress is chosen, n is the stress exponent, Q is the activation energy for deformation, R is the universal gas constant (8.314 J/mol·K), and T is the absolute deformation temperature.

In order to determine the value of α in Eq. (1), the other two equations are required. At low stresses, Eq. (1) reduces to a power

Table 1

Experimental and theoretical determination of alpha and beta phase volume fractions of LAZ922 alloy at temperatures of 473–523 K.

	$(V_{\alpha}/V_{\beta})^a/\%$	(a)	(b)	(c)	(d)	$(V_{\alpha}/V_{\beta})^b/\%$	$(V_{\alpha}/V_{\beta})^c/\%$
Fig. 2	37.5/62.5	43.7/56.3	36.2/63.8	33.8/66.2	37.8/62.2	21.7/78.3	
Fig. 3	29.3/70.7	44.2/55.8	32.4/67.6	35.1/64.9	35.3/64.7	21.7/78.3	

^a Experimental phase volume fraction.

^b Mean phase volume fraction.

^c Theoretical phase volume fraction determined by lever rule [24].

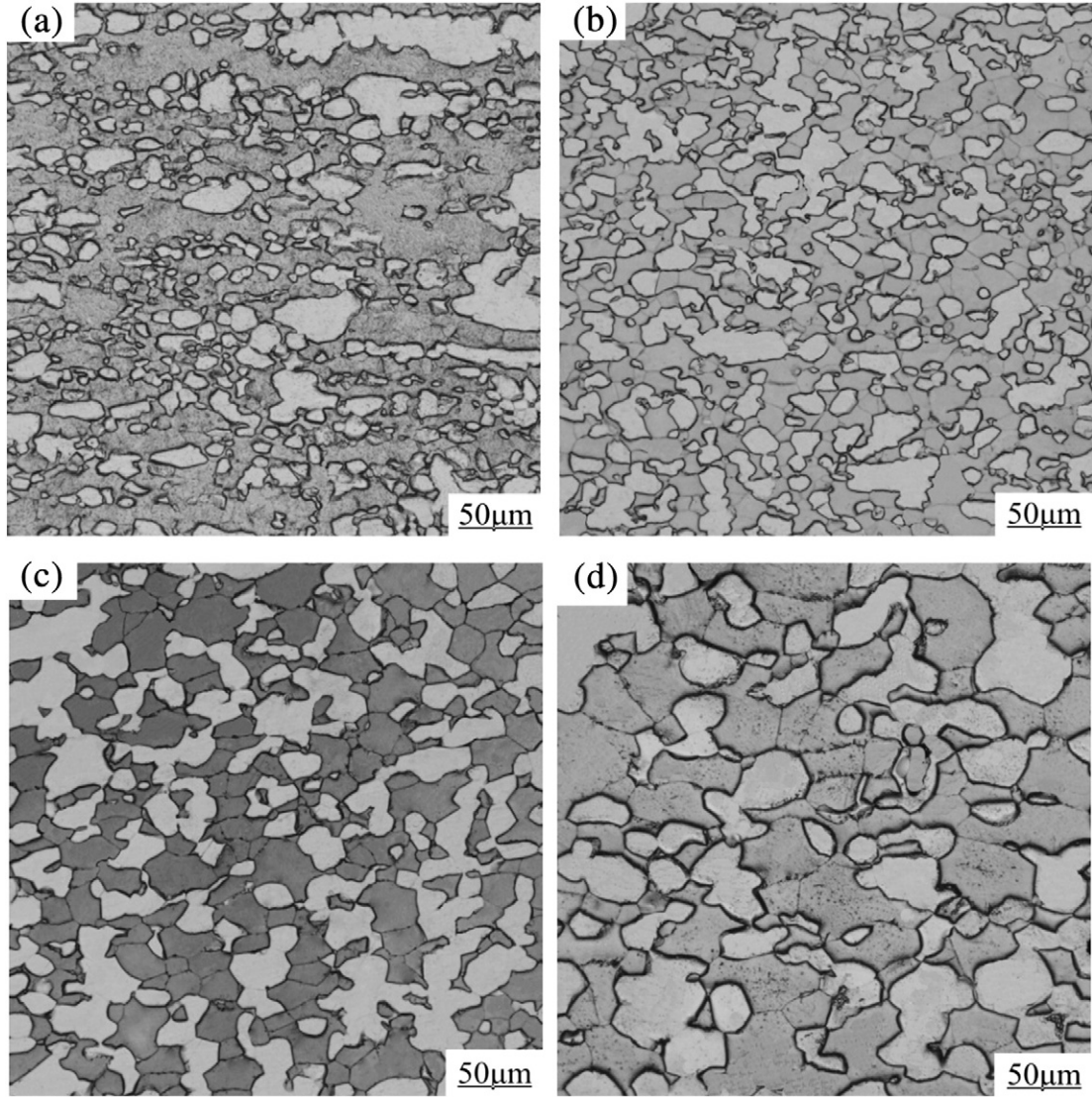


Fig. 4. Microstructures of LAZ922 alloy at the deformation temperature of 573 K with different strain rates and grain sizes/elongations to failure. (a) $1.67 \times 10^{-2} \text{ s}^{-1}$, 13.28 μm /128.6%, (b) $1.67 \times 10^{-3} \text{ s}^{-1}$, 16.81 μm /175%, (c) $5 \times 10^{-4} \text{ s}^{-1}$, 29.37 μm /300%, and (d) $1.67 \times 10^{-4} \text{ s}^{-1}$, 33.38 μm /566.7%.

relationship (Eq. (2)), and at high stresses to an exponential relationship (Eq. (3)):

$$\dot{\epsilon} = A_1 \sigma^{n_1} \exp(-Q/(RT)) \quad (2)$$

$$\dot{\epsilon} = A_2 \exp(\beta\sigma) \exp(-Q/(RT)) \quad (3)$$

where A_1 , A_2 , n_1 , and β are the material constants.

Taking natural logarithms for Eqs. (1)–(3) gives

$$\ln \dot{\epsilon} = \ln(A_1) + n_1 \ln \sigma - Q/(RT) \quad (4)$$

$$\ln \dot{\epsilon} = \ln(A_2) + \beta\sigma - Q/(RT) \quad (5)$$

$$\ln \dot{\epsilon} = n \ln[\sinh(\alpha\sigma)] + \ln A - Q/(RT) \quad (6)$$

where $\alpha = \beta/n_1$, and n_1 , β , and n are the slopes of Eqs. (4)–(6), respectively.

Fig. 8 shows the relation curves for determination of material constants. Based on Fig. 8(a) and (b), the n_1 and β values were determined as 3.679 and 0.169 via the calculation of mean slope of the curves. Thus, $\alpha = 0.0459$. According to Fig. 8(c), the n value was determined as 1.949 by the mean slope of the curves.

The activation energy for deformation, Q , can be expressed as follows according to Eq. (6):

$$Q = R \left[\frac{\partial \ln \dot{\epsilon}}{\partial \ln[\sinh(\alpha\sigma)]} \right]_T \left[\frac{\partial \ln[\sinh(\alpha\sigma)]}{\partial (1/T)} \right]_{\dot{\epsilon}} = Rnp \quad (7)$$

where p is the mean slope of $\ln[\sinh(\alpha\sigma)] - 1/T$ curve and can be obtained by Fig. 8(d). Thus, $p = 8.709$. Substitution of n and p values into Eq. (7), average activation energy Q was calculated to be 141.12 kJ/mol.

Eq. (1) can be expressed by the Z parameter:

$$Z = \dot{\epsilon} \exp(Q/(RT)) = A[\sinh(\alpha\sigma)]^n. \quad (8)$$

Taking natural logarithm of Eq. (8) gives

$$\ln Z = \ln A + n \ln[\sinh(\alpha\sigma)]. \quad (9)$$

To get A value, the curve of $\ln Z - \ln[\sinh(\alpha\sigma)]$ relation must be obtained. Fig. 9(a) shows the relationship between $\ln Z$ and $\ln[\sinh(\alpha\sigma)]$. The slope of the curve was calculated as $n = 1.905$, and $\ln A = 22.502$ was obtained via $\ln Z$ value at the zero point of $\ln[\sinh(\alpha\sigma)]$. The

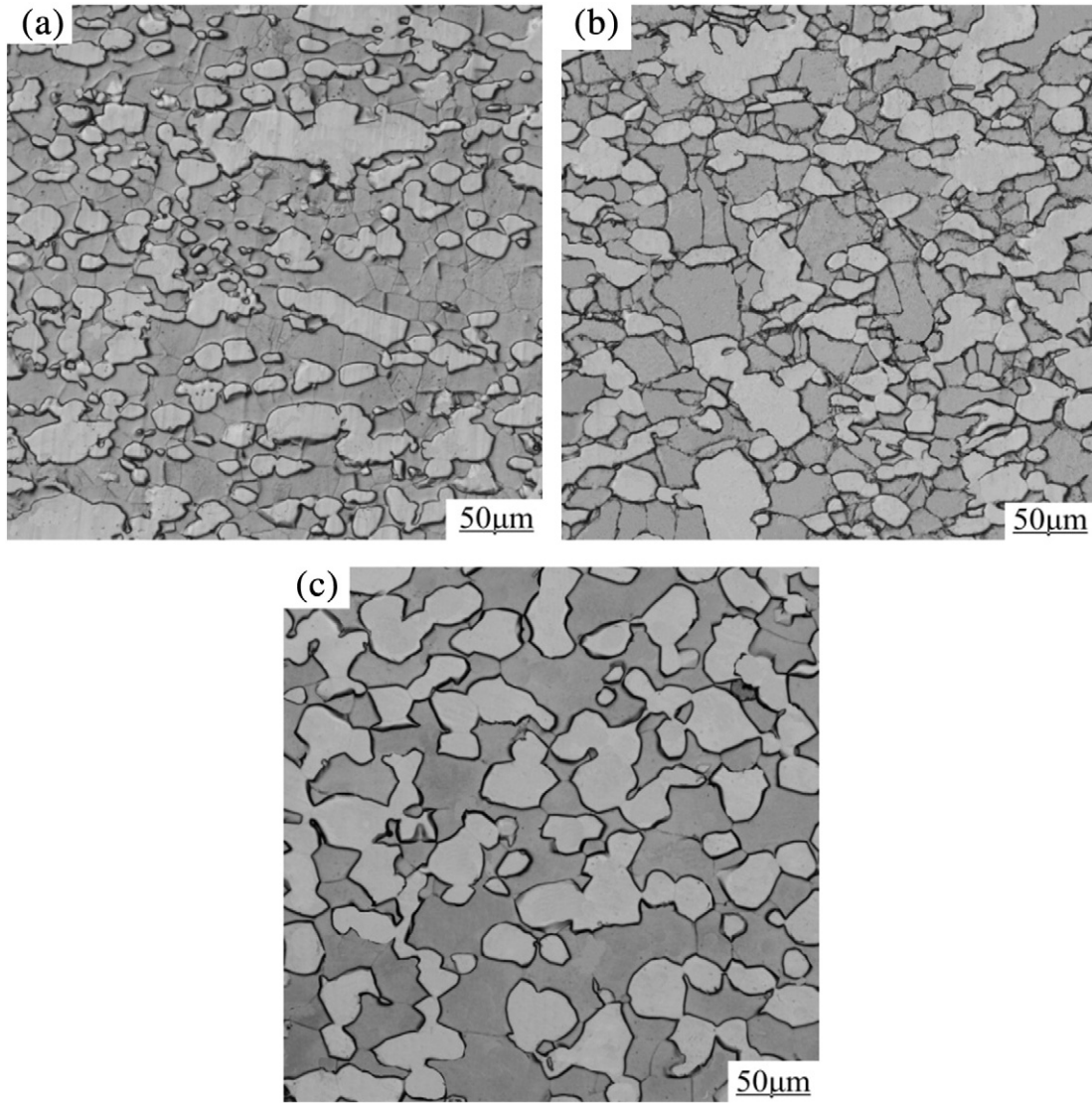


Fig. 5. Microstructures of LAZ922 alloy at the deformation temperature of 623 K with different strain rates and grain sizes/elongations to failure. (a) $1.67 \times 10^{-3} \text{ s}^{-1}$, 14.22 μm /157.1%, (b) $1.67 \times 10^{-3} \text{ s}^{-1}$, 20.67 μm /375%, and (c) $5 \times 10^{-4} \text{ s}^{-1}$, 34.36 μm /262.5%.

correlation coefficient (R) is 0.968. Therefore, constitutive equation in Eq. (1) can be expressed as the following:

$$\dot{\varepsilon} = e^{22.502} [\sinh(0.0459\sigma)]^{1.905} \exp\left(\frac{-141120.5}{RT}\right). \quad (10)$$

By mathematical treatment, flow stress can be expressed by the Z parameter.

$$\sigma = (1/\alpha) \ln \left\{ \left(\frac{Z}{A} \right)^{1/n} + \left[\left(\frac{Z}{A} \right)^{2/n} + 1 \right]^{1/2} \right\}.$$

Hence, the following constitutive equation is obtained.

$$\sigma = \left(\frac{1}{0.0459} \right) \ln \left\{ \left(\frac{Z}{5.922 \times 10^9} \right)^{1/1.905} + \left[\left(\frac{Z}{5.922 \times 10^9} \right)^{2/1.905} + 1 \right]^{1/2} \right\} = f(Z). \quad (11)$$

Fig. 9(b) shows the results of comparison between the calculated stress and the measured stress. Good agreement is achieved with a correlation coefficient of 0.981.

3.4. Dynamic recrystallization kinetics

To obtain the DRX kinetics model, we must firstly know the characteristic points of flow stress–strain curve, as shown in Fig. 10. There are two distinct dynamic softening mechanisms, i.e., dynamic recovery (DRV) and DRX, during hot deformation. Fig. 10(a) shows the typical DRV and DRX curves. For DRV curve, the flow stress increases with strain and finally reaches a saturation stress (σ_{vs}), whereas for DRX curve, when the strain (ε) exceeds the critical strain (ε_c) and corresponding stress (σ) exceeds the critical stress (σ_c), DRX takes place. When the strain exceeds the peak strain (ε_p) and corresponding stress exceeds the peak stress (σ_p), flow stress drops gradually to the steady-state stress (σ_{ss}) because of DRX softening.

The critical stress (σ_c) for the initiation of DRX can be determined by the inflection point of θ – σ curve, where θ is the strain hardening rate, $\theta = d\sigma / d\varepsilon$ [29,30]. Fig. 10(b) shows the relationship between strain hardening rate (θ) and stress (σ). The saturation stress σ_{vs} is defined by the extrapolation of the θ – σ curve to $\theta = 0$ using the tangential line drawn from the inflection point. θ – σ curve intersects at $\theta = 0$ horizontal line and the intersection points are the peak stress σ_p and the steady state stress σ_{ss} .

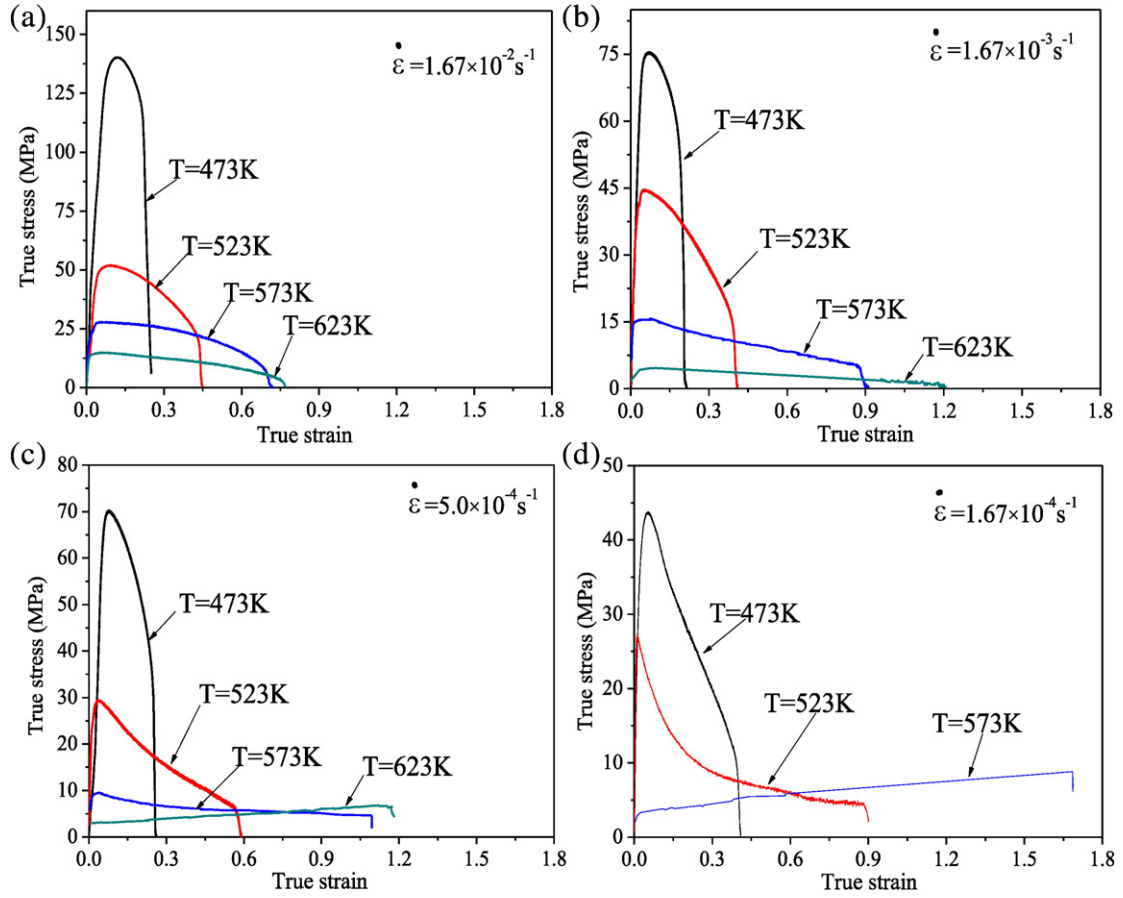


Fig. 6. True stress-true strain curves of LAZ922 alloy at different temperatures at the same initial strain rates. (a) $1.67 \times 10^{-2} \text{ s}^{-1}$, (b) $1.67 \times 10^{-3} \text{ s}^{-1}$, (c) $5 \times 10^{-4} \text{ s}^{-1}$, and (d) $1.67 \times 10^{-4} \text{ s}^{-1}$.

θ - σ curve can be described by the following equation [31]:

$$\theta = B_1\sigma^3 + B_2\sigma^2 + B_3\sigma + B_4 \quad (12)$$

where B_1 , B_2 , B_3 , and B_4 are constants for different deformation conditions.

Differentiating Eq. (12) twice with respect to σ , we set the expression to zero. The critical stress of DRX is obtained.

$$\frac{d^2\theta}{d\sigma^2} = 6B_1\sigma_c + 2B_2 = 0 \Rightarrow \sigma_c = -B_2/3B_1. \quad (13)$$

Fig. 11 shows the relationship between the strain hardening rate and the stress under different deformation conditions. Table 2 shows the characteristic values fitted for the strain hardening rate versus the stress.

By regression analysis, the relationships between the critical stress (strain) and the peak stress (strain) were determined:

$$\sigma_c = 0.67\sigma_p + 1.19. \quad (14)$$

$$\varepsilon_c = 0.40\varepsilon_p. \quad (15)$$

In addition, by mathematical average of the critical stress and the peak stress in Table 2, the following relation can also be obtained:

$$\sigma_c = 0.70\sigma_p. \quad (16)$$

DRX volume fraction can be described by Avrami equation:

$$X_{\text{DRX}} = 1 - \exp \left[-t \left(\frac{\varepsilon - \varepsilon_c}{\varepsilon_p} \right)^k \right] \quad (17)$$

where X_{DRX} is the DRX volume fraction, t is the material constant, and k is the Avrami exponent.

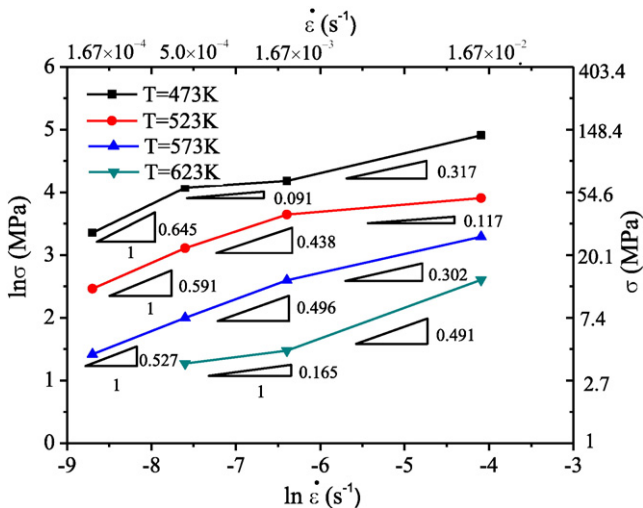


Fig. 7. Relationship between $\ln\sigma$ and $\ln\dot{\varepsilon}$ at a true strain of 0.2.

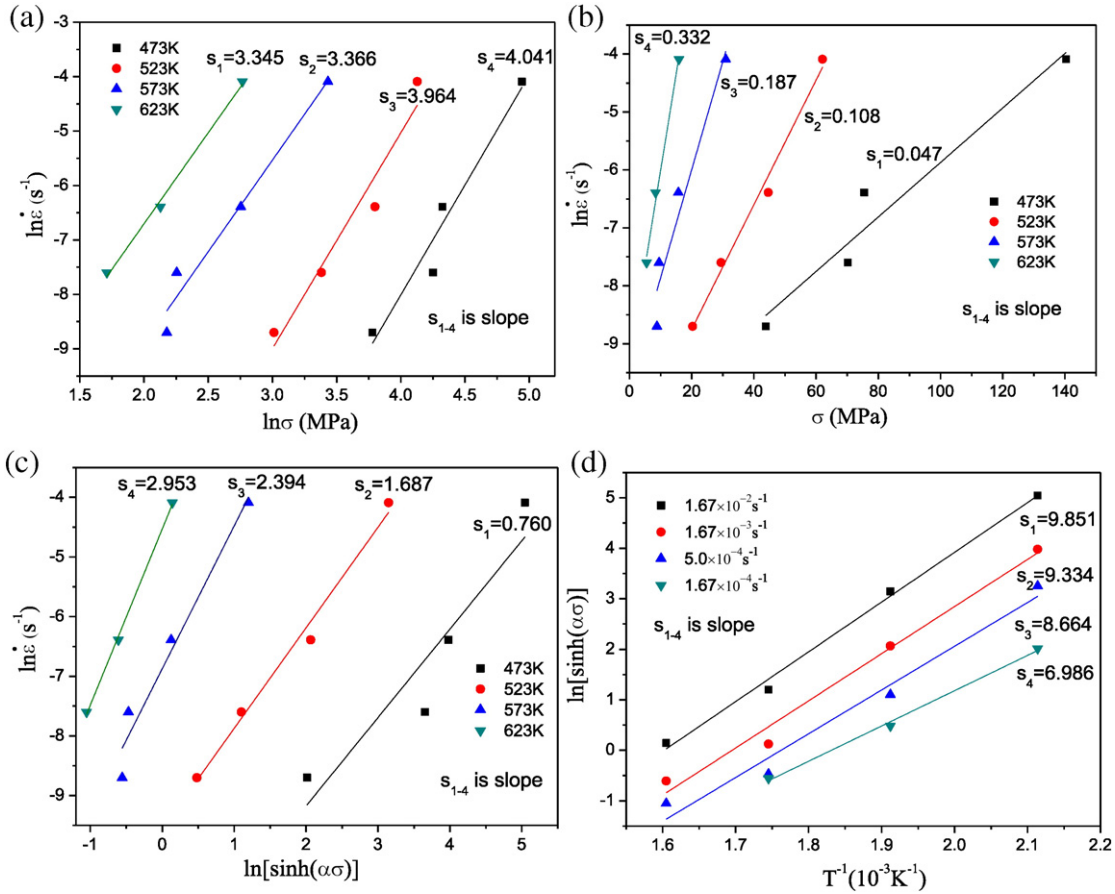


Fig. 8. Relationship between (a) $\ln \dot{\epsilon}$ and $\ln \sigma$, (b) $\ln \dot{\epsilon}$ and σ , (c) $\ln \dot{\epsilon}$ and $\ln[\sinh(\alpha\sigma)]$, and (d) $\ln[\sinh(\alpha\sigma)]$ and $1/T$.

X_{DRX} can be determined by the following relation [32]:

$$X_{DRX} = \frac{\sigma_{vs}^2 - \sigma_c^2}{\sigma_{vs}^2 - \sigma_{ss}^2}. \quad (18)$$

Because some stress–strain curves in Fig. 6 do not have steady-state stage, their steady-state stresses cannot be determined and the application of Eq. (18) is restricted, probably due to the hot tensile deformation instead of hot compression because flow stress curve of hot compression often exhibits steady-state stage. Here, two stress–strain curves corresponding to full DRX were chosen. The steady-state stress σ_{ss} at

573 K with strain rates of 1.67×10^{-3} and $5 \times 10^{-4} s^{-1}$ were 5.1 and 4.7 MPa, respectively, according to Fig. 6(b) and (c). Substitution of σ_{vs} , σ_{ss} , ϵ_c , and ϵ_p in Table 2 into Eqs. (17) and (18), the mean values of the material constant t and k were calculated as $t = 0.304$ and $k = 0.989$, respectively. Thus, the kinetics equation of DRX evolution is expressed as the following:

$$X_{DRX} = 1 - \exp[-0.304(\epsilon/\epsilon_p - 0.40)^{0.989}]. \quad (19)$$

Fig. 12 shows the DRX volume fraction as a function of true strain. It can be seen that the DRX volume fraction increases with increasing the strain.

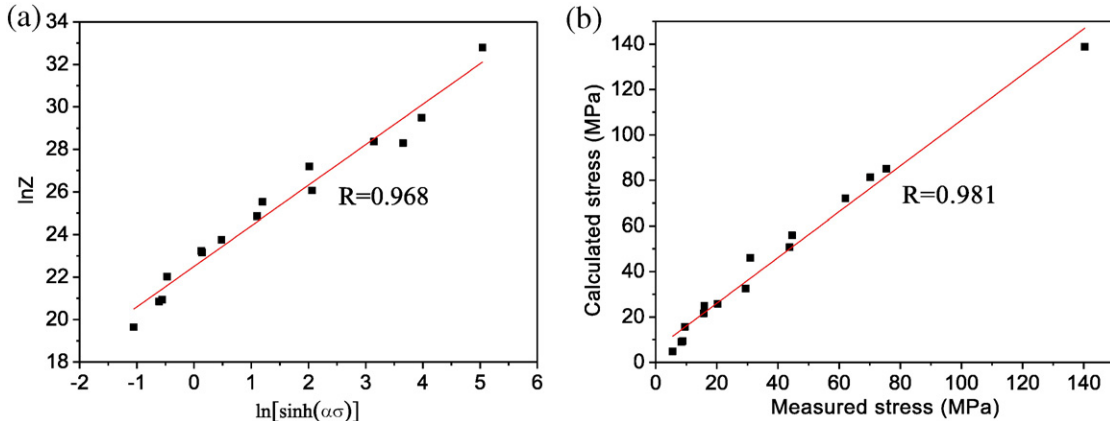


Fig. 9. Relationship between (a) $\ln Z$ and $\ln[\sinh(\alpha\sigma)]$ and (b) calculated stress and measured stress.

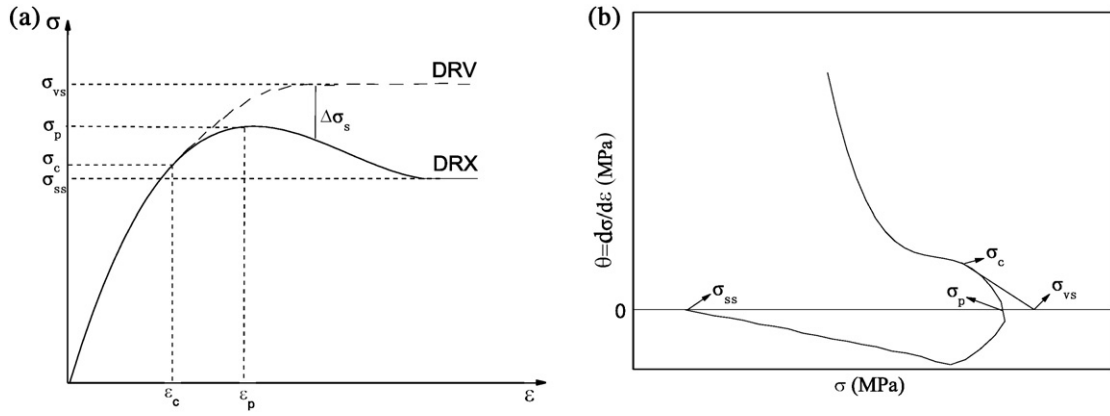


Fig. 10. Schematic diagrams of (a) typical DRV and DRX curves for defining various strain and stress parameters and (b) relationship between strain hardening rate (θ) and stress (σ).

4. Discussion

4.1. Microstructures and flow stress curves

4.1.1. Importance of deformation conditions to DRX

In Sections 3.1.2 and 3.2, it is found that full DRX difficulty takes place at relatively low temperature and/or higher strain rate but full DRX easily takes place at higher temperature and/or lower strain rate. This means that DRX is very sensitive to the deformation conditions and is a thermally activated process. With the increase of deformation temperature, external thermal energy is inputted into the deformation body, atomic diffusion speeds up, the number of slip system increases, the mobility of dislocations increases, and hence flow stress decreases. Thus, DRX easily occurs. With the decrease of strain rate, the time for reaching the same deformation strain prolongs, atomic diffusion

enhances, the number of dislocations decreases, and hence flow stress decreases. Thus, DRX easily takes place. On the contrary, at relatively low temperature and/or higher strain rate, the thermal activation process slows down and only partial DRX occurs. Thus, at 473 and 523 K with strain rates of less than $1.67 \times 10^{-4} \text{ s}^{-1}$, partial DRX or continuous DRX takes place, whereas at 573 and 623 K at most strain rates, complete DRX followed by pronounced dynamic grain growth occurs. Moreover, in most cases, the elongation to failure increases with increasing the temperature at the constant strain rate because of the acceleration of DRX.

4.1.2. Causes of flow softening and peculiar hardening phenomena at the third stage

Most flow stress curves at the third stage in Fig. 6 exhibit flow softening, except the peculiar hardening at 573 K and $1.67 \times 10^{-4} \text{ s}^{-1}$

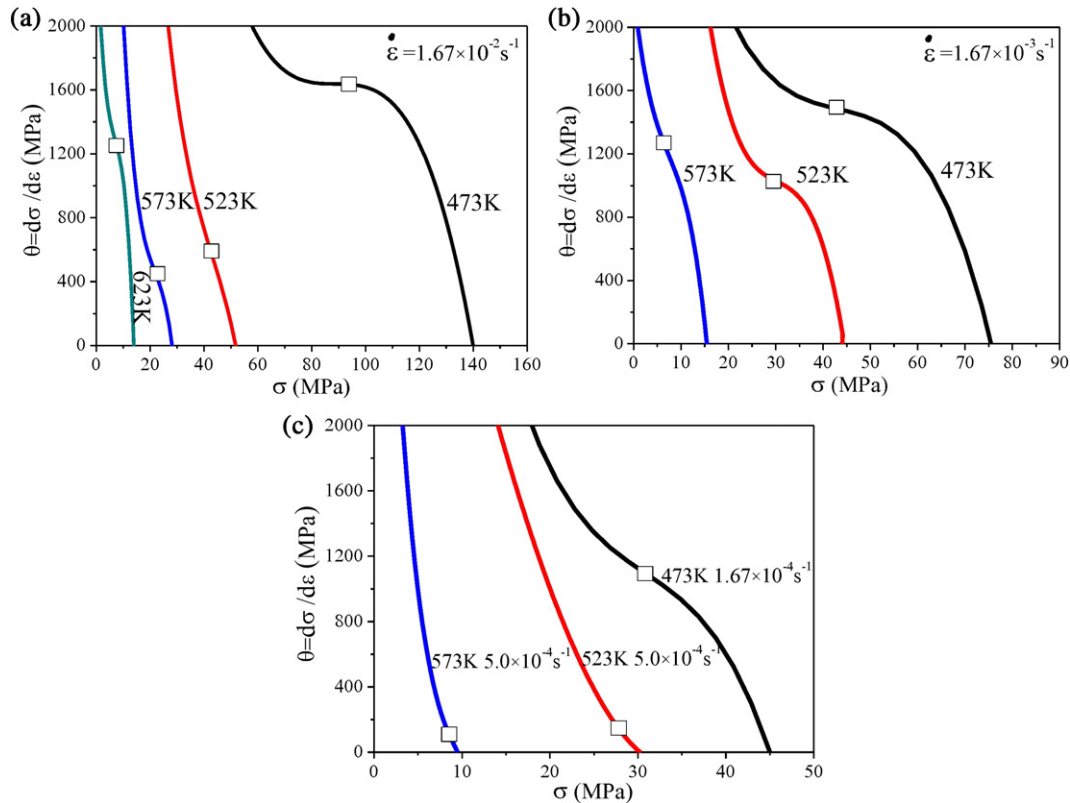


Fig. 11. Strain hardening rate as a function of flow stress under different deformation conditions. (a) $1.67 \times 10^{-2} \text{ s}^{-1}$, 473–623 K, (b) $1.67 \times 10^{-3} \text{ s}^{-1}$, 473–573 K, and (c) 1.67×10^{-4} – $5.0 \times 10^{-4} \text{ s}^{-1}$, 473–573 K. Symbol "□" indicates the inflection point.

Table 2
Characteristic values fitted for the strain hardening rate versus the stress.

$\dot{\epsilon}/s^{-1}$	T/K	B_1	B_2	B_3	B_4	σ_c/MPa	σ_p/MPa	σ_{vs}/MPa	ϵ_c	ϵ_p
1.67×10^{-2}	473	-1.00×10^{-2}	2.92	-262.22	9.19×10^3	97.27	140.34	173.56	0.046	0.122
1.67×10^{-2}	523	-1.26×10^{-1}	16.27	-754.78	1.30×10^4	43.04	52.05	53.24	0.043	0.115
1.67×10^{-2}	573	-6.73×10^{-1}	43.76	-991.77	8.26×10^3	21.67	27.95	32.15	0.016	0.061
1.67×10^{-2}	623	-2.59	54.16	-437.56	2.58×10^3	6.97	14.91	20.34	0.005	0.080
1.67×10^{-3}	473	-3.68×10^{-2}	4.76	-211.71	4.72×10^3	43.12	75.50	83.10	0.027	0.085
1.67×10^{-3}	523	-2.8×10^{-1}	25.39	-781.7	9.20×10^3	30.23	44.52	49.12	0.018	0.053
1.67×10^{-3}	573	-9.5×10^{-1}	18.93	-190.44	1.96×10^3	6.64	15.71	24.85	0.002	0.008
5.0×10^{-4}	523	-3.06×10^{-1}	27.27	-874.41	1.00×10^4	29.71	30.41	32.27	0.038	0.098
5.0×10^{-4}	573	-5.06	147.24	-1532.43	5.61×10^3	9.70	10.50	11.43	0.031	0.089
1.67×10^{-4}	473	-2.04×10^{-1}	18.83	-615.79	8.16×10^3	30.77	43.80	57.12	0.016	0.055

and at 623 K and $5 \times 10^{-4} s^{-1}$. For deformation at room temperature, the strength of grain boundary is stronger than the strength of grain interior, whereas for deformation at high temperature, the strength of grain boundary is weaker than the strength of grain interior. On one hand, in Figs. 2 and 3, at temperatures of 423 and 523 K, grains are refined due to partial DRX under applied stress. In Figs. 4 and 5, equiaxed grains are formed from the initial elongated grains, which results in the decrease in flow stress and the flow softening of full DRX. For deformation at elevated temperatures, the formation and growth of smaller new DRX grains lead to the annihilation of dislocations, which decreases the flow stress, and due to grain refinement caused by DRX, the number of grain boundary increases and hence the flow stress decreases. For this reason, flow softening at the third stage appears; on the other hand, according to Eqs. (23) and (25) in Section 4.2, the dislocation density is proportional to the square of stress and the number of dislocations inside a grain is proportional to the grain size. Bigger grain sizes caused by the deformation-induced grain growth (DIGG) at 573 K and $1.67 \times 10^{-4} s^{-1}$ and at 623 K and $5 \times 10^{-4} s^{-1}$ result in the reduction of number of grain boundary, the increase of number of dislocations inside the grain, the increase of dislocation density, and hence the increase in flow stress with increasing strain. For this reason, peculiar strain hardening at the third stage appears.

Above-mentioned DIGG is analyzed as follows. Hot tensile deformation process is equivalent to a “straining” annealing process in which atomic diffusion plays an important role in DIGG. Grain growth is a result of boundary migration. The boundary migration velocity or the velocity of grain boundary movement, v , obeys the following relation:

$$v = M' F \quad (20)$$

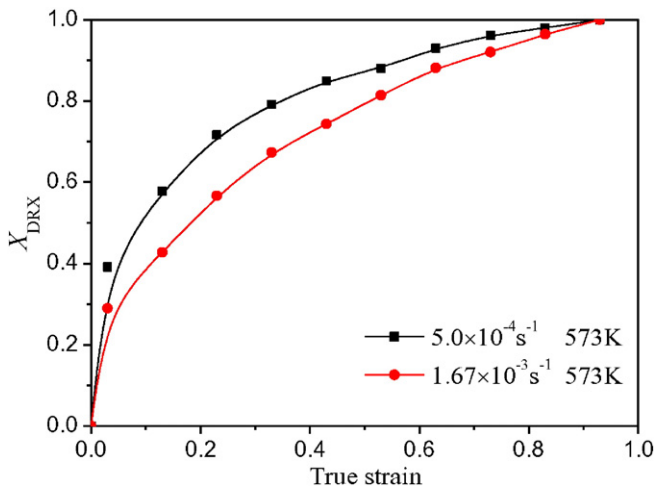


Fig. 12. DRX volume fraction as a function of true strain.

where F is the driving force and M' is the atomic mobility in the grain boundary.

$$M' = D_{gb} / (k_B T) \quad (21)$$

where D_{gb} is the grain boundary diffusion coefficient (GBDC), k_B is Boltzmann's constant, and T is the absolute temperature.

The GBDC for single phase polycrystalline material D_{gb} is given by

$$D_{gb}(D_{gb}(\alpha) \text{ and } D_{gb}(\beta)) = 10^{-4} \exp(-Q_{gb}/RT), \quad Q_{gb} = 6.93RT_m \quad 0.22 < T/T_m < 0.42; \quad 9.35RT_m \quad 0.42 < T/T_m < 1.0 \quad (22)$$

[33]

Where T_m is the melting point of α (5.7Li) phase and β (11Li) phase, 861 K and 867 K, respectively, according to Mg–Li phase diagram [24].

To identify the difference of the GBDCs of α phase and β phase from those of Mg, Al, and Ni metals, the GBDCs of Mg, Al, and Ni were chosen [34]. Table 3 shows the calculated results of grain boundary diffusion coefficients of α phase, β phase, Mg, Al, and Ni at 573 K. It is noted that the GBDC values of α phase and β phase in Mg–Li alloy are 2.47 and 2.24 times as much as the GBDC value of Mg, 41.41 and 37.59 times as much as the GBDC value of Al, and 343,913 and 312,174 times as much as the GBDC value of Ni, respectively. According to Eq. (21), the atomic mobility M' is proportional to the GBDC D_{gb} . This means that bigger GBDC values of α phase and β phase in Mg–Li alloy lead to faster atomic mobility or atomic diffusion velocity. According to Eq. (20), the boundary migration velocity v is proportional to the atomic mobility M' . This means that faster atomic mobility leads to faster boundary migration. Due to extremely fast boundary migration velocities of α phase and β phase in LAZ922 alloy at 573 K, DIGG is easier to take place. Moreover, the DIGG of the present alloy at 623 K follows the same rule. That is the atomic diffusion reason of the DIGG.

4.1.3. Explanation of the causes of 566.7% superplasticity

Even after more than 500% elongation, the grain shape in Fig. 4(d) still keeps its equiaxed state. Typical superplasticity of materials was defined as elongation to failure (δ) more than 400% and m value around 0.5 [35], under which condition GBS is the deformation mechanism. Now, experimental δ (566.7%) and m (0.527) of LAZ922 alloy at 573 K and $1.67 \times 10^{-4} s^{-1}$ in Section 3.2 conform to this definition and according to its equiaxed grain morphology, we conclude that

Table 3
Calculation of grain boundary diffusion coefficients of α phase, β phase, Mg, Al, and Ni.

$D_{gb}/m^2 s^{-1}$	α (5.7Li) phase ^a $\times 10^{-11}$	β (11Li) phase ^a $\times 10^{-11}$	Mg ^b $\times 10^{-11}$	Al ^b $\times 10^{-12}$	Ni ^b $\times 10^{-16}$
573 ^c	7.91	7.18	3.20	1.91	2.30

^a Calculated by Eq. (22).

^b Calculated according to Ref. [34].

^c $T = 573$ K.

Table 4

Relevant parameters and calculated results of critical peak dislocation density and critical peak stress.

$G/\times 10^4$ MPa	$b^a/\times 10^{-10}$ m	$\gamma_{gb}^b/\text{J m}^{-2}$	$wD_{0gb}^a/\times 10^{-12}$ $\text{m}^3 \text{s}^{-1}$	$Q_{gb}^a/\text{kJ mol}^{-1}$	$E/\times 10^{-10}$ Jm^{-1}	$l^c/\times 10^{-9}$ m	$\rho_p/\times 10^{15}\text{m}^{-2}$	$\rho_{cp}/\times 10^{15}\text{m}^{-2}$	σ_{cp}/MPa
1.51	3.21	1.0	5.0	92	7.77	1.28	8.37	6.08	119

 $T = 473 \text{ K}$, $\dot{\epsilon} = 1.67 \times 10^{-2} \text{ s}^{-1}$, $\sigma_p = 140 \text{ MPa}$, $k_1 = 0.70$, $k_b = 1.38 \times 10^{-23} \text{ JK}^{-1}$, $B = 10$.^a Data from Ref. [34].^b Data from Ref. [46].^c $l = 4b$.

GBS dominates its rate-controlling mechanism. The activation energy for deformation in Section 3.3 is 141.12 kJ/mol, slightly higher than the lattice diffusion activation energy of Mg, 135 kJ/mol [36]. This is because as shown in Fig. 1, the second phase strengthening (AlLi phase) and solid solution strengthening (Zn element dissolved in the matrix) raise the activation energy for deformation. Thus, lattice diffusion is its diffusion mechanism. Based on the microstructures in Figs. 1(a) and 4(d), the microstructural evolution in LAZ922 alloy under above-mentioned condition is suggested as follows: owing to the hot deformation under applied stress, the elongated grains are transformed into equiaxed grains and low angle grain boundary is changed into high angle grain boundary. These equiaxed grains undergo “straining” and GBS occurs. GBS leads to boundary (α/α , α/β , and β/β interfaces) migration and DIGG takes place. The hardening caused by the DIGG strengthens the uniform deformation. Therefore, 566.7% superplasticity is achieved. Its rate-controlling mechanism is DRX and GBS controlled by the lattice diffusion.

4.2. Constitutive equation and DRX kinetics

Dislocation density is an important variable during plastic deformation and its theory and experimental investigation attract researcher's attention [37–40]. First, an attempt is made to establish the constitutive relationship of dislocation density and number of dislocations with Z parameter. The dislocation density obeys the following relation [34,41]:

$$\rho = B(Gb)^{-2}\sigma^2 \quad (23)$$

where ρ is the dislocation density, B is a dimensionless constant, σ is the applied stress, G is the shear modulus, and b is the magnitude of Burgers vector.

The number of dislocations inside a grain is expressed as the following [42]:

$$N = (1-\nu)L\pi\tau/(Gb) \quad (24)$$

where N is the mean number of dislocations inside the grain, ν is Poisson's ratio, L is equivalent to the average linear intercept grain size, $L = d$, τ is the shear stress acting on the slip plane inside the grain, $\tau = \sigma/\sqrt{3}$.

Substitution of $L = d$ and $\tau = \sigma/\sqrt{3}$ into Eq. (24) gives

$$N = 1.81(1-\nu)(d\sigma/(Gb)). \quad (25)$$

Substitution of Eq. (11) into Eqs. (23) and (25) gives

$$\rho = B(Gb)^{-2}[f(Z)]^2 \quad (26)$$

$$N = 1.81(1-\nu)(d/(Gb))f(Z) \quad (27)$$

where $Z = \dot{\epsilon} \exp(-Q/(RT))$.

Eqs. (26) and (27) show the relationship between the dislocation density and Z parameter and the relationship between the mean number of dislocations inside the grain and Z parameter, respectively.

Second, the critical conditions of peak dislocation density and peak stress are established. It is generally recognized that the critical stress for the initiation of DRX obeys the following relation:

$$\sigma_c = k_1\sigma_p \quad (28)$$

where k_1 is a material constant, $0 < k_1 < 1$.

Substitution of Eq. (23) into Eq. (28) gives

$$\rho_c = k_1^2\rho_p \quad (29)$$

where ρ_c is the critical dislocation density for the initiation of DRX, and ρ_p is the critical peak dislocation density.

According to Ref. [43], ρ_c can be expressed as the following:

$$\rho_c = \left(\frac{20\gamma_{gb}\dot{\epsilon}}{3blME^2}\right)^{1/3} \quad (30)$$

where γ_{gb} is the grain boundary energy, b is the magnitude of Burgers vector, l is the dislocation mean-free path, $3-5b$ [44], M is the grain boundary mobility, and E is the dislocation line energy, 0.5 Gb^2 .

Combining Eq. (29) with Eq. (30) gives

$$\rho_{cp} = \frac{1}{k_1^2} \left(\frac{20\gamma_{gb}\dot{\epsilon}}{3blME^2}\right)^{1/3}. \quad (31)$$

Eq. (31) is the critical peak dislocation density condition for the initiation of DRX.

Substitution of Eq. (31) into Eq. (23) gives

$$\sigma_{cp} = \frac{Gb}{k_1 B^{0.5}} \left(\frac{20\gamma_{gb}\dot{\epsilon}}{3blME^2}\right)^{1/6}. \quad (32)$$

Eq. (32) is the critical peak stress condition for the initiation of DRX. Because σ_p is more convenient to be used than σ_c , Eq. (32) will play an important role in determining the critical peak stress. Only after the peak dislocation density ρ_p and the peak stress σ_p exceed the critical peak dislocation density ρ_{cp} and the critical peak stress σ_{cp} can the DRX be initiated.

Third, the critical conditions of peak dislocation density and peak stress are estimated in the present alloy. The shear modulus of Mg is given by [34]

$$G(\text{MPa}) = 1.66 \times 10^4 \left\{ 1 - 0.49 \left(\frac{T-300}{924} \right) \right\}. \quad (33)$$

The grain boundary mobility M is expressed as the following [45]:

$$M = \frac{wD_{gb}b}{k_B T} = \frac{bwD_{0gb} \exp(-Q_{gb}/(RT))}{k_B T} \quad (34)$$

where w is the grain boundary thickness, D_{0gb} is the pre-exponential factor, and Q_{gb} is the grain boundary diffusion activation energy.

As shown in Fig. 6(a), the experimental peak stress of the present alloy at 473 K and $1.67 \times 10^{-2} \text{ s}^{-1}$ was determined as 140 MPa. Table 4 shows the parameters and calculated results of critical peak

dislocation density and critical peak stress [46]. The peak dislocation density ($8.37 \times 10^{15} \text{ m}^{-2}$) is greater than the critical peak dislocation density ($6.08 \times 10^{15} \text{ m}^{-2}$) and the peak stress (140 MPa) is larger than the critical peak stress (119 MPa), indicating that DRX is initiated under the experimental condition. The theoretical criterion is consistent with the experimental microstructure of partial DRX in Fig. 2(a).

5. Conclusions

1. TEM and XRD examinations show that the initial microstructure of the present alloy consists of α -Mg, β -Li and AlLi phases. The temperature and strain rate have a considerable effect on the hot deformation process. Microstructural study reveals that at the temperatures of 473 and 523 K with strain rates of less than $1.67 \times 10^{-4} \text{ s}^{-1}$, partial DRX or continuous DRX takes place, whereas at the temperatures of 573 and 623 K at most strain rates, complete DRX and pronounced dynamic grain growth occur. Calculation shows that rapid atomic diffusion velocities of α and β phases at 573 K lead to rapid grain boundary migration and dynamic grain growth.
2. The maximum superplasticity of 566.7% was demonstrated in Mg–9.3Li–1.79Al–1.61Zn alloy at the temperature of 573 K and the strain rate of $1.67 \times 10^{-4} \text{ s}^{-1}$. The strain rate sensitivity exponent was 0.527. Its rate-controlling mechanism is dynamic recrystallization and grain boundary sliding controlled by lattice diffusion.
3. A constitutive equation was established by regression analysis of Arrhenius type hyperbolic sine function and the activation energy for deformation of the present alloy was determined as 141.12 kJ/mol, slightly higher than the lattice diffusion activation energy of Mg, 135 kJ/mol. The predicted results are in good agreement with the measured results with high correlation coefficients. In addition, constitutive relationships between dislocation variables (dislocation density and number of dislocations) and Zener–Hollomon parameter were modeled.
4. The critical parameters at characteristic points of flow stress curves were determined. The relationship between the DRX volume fraction and the strain was established by using Avrami type equation. The conditions of critical peak dislocation density and critical peak stress for the initiation of DRX were derived. Calculation reveals that the theoretical criterion is consistent with the experimental microstructure.

Acknowledgments

The authors are indebted to the financial support of the key project of National Natural Science Foundation of China under Grant No. 51334006.

References

- [1] R. Mahmudi, M. Shalabafi, M. Karami, A.R. Geranmayeh, Effect of Li content on the indentation creep characteristics of cast Mg–Li–Zn alloys, *Mater. Des.* 75 (2015) 184–190.
- [2] Y. Zeng, B. Jiang, R.H. Li, J.J. He, X.S. Xia, F.S. Pan, Effect of Li content on microstructure, texture and mechanical properties of cold rolled Mg–3Al–1Zn alloy, *Mater. Sci. Eng. A* 631 (2015) 189–195.
- [3] D.K. Xu, B.J. Wang, C.Q. Li, T.T. Zu, E.H. Han, Effect of icosahedral phase on the thermal stability and aging response of a duplex structured Mg–Li alloy, *Mater. Des.* 69 (2015) 124–129.
- [4] X.Y. Guo, R.Z. Wu, J.H. Zhang, B. Liu, M.L. Zhang, Influences of solid solution parameters on the microstructure and hardness of Mg–9Li–6Al and Mg–9Li–6Al–2Y, *Mater. Des.* 53 (2014) 528–533.
- [5] Y. Yang, X.D. Peng, H.M. Wen, G.B. Wei, W.D. Xie, E.J. Lavernia, Microstructure and mechanical behavior of Mg–10Li–3Al–2.5Sr alloy, *Mater. Sci. Eng. A* 611 (2014) 1–8.
- [6] Y. Yang, X.D. Peng, H.M. Wen, B.L. Zheng, Y.Z. Zhou, W.D. Xie, et al., Influence of extrusion on the microstructure and mechanical behavior of Mg–9Li–3Al–xSr alloys, *Metall. Mater. Trans. A* 44 (2013) 1101–1113.
- [7] F.R. Cao, F. Xia, H.L. Hou, H. Ding, Z.Q. Li, Effects of high-density pulse current on mechanical properties and microstructure in a rolled Mg–9.3Li–1.79Al–1.61Zn alloy, *Mater. Sci. Eng. A* 637 (2015) 89–97.
- [8] Y. Han, H. Wu, W. Zhang, D.N. Zou, G.W. Liu, G.J. Qiao, Constitutive equation and dynamic recrystallization behavior of as-cast 254Mo super-austenitic stainless steel, *Mater. Des.* 69 (2015) 230–240.
- [9] E.S. Puchi-Cabrera, J.D. Guerin, M. Dubar, M.H. Staia, J. Lesage, D. Chicot, Constitutive description for the design of hot-working operations of a 20MnCr5 steel grade, *Mater. Des.* 62 (2014) 255–264.
- [10] H.B. Zhang, K.F. Zhang, S.S. Jiang, Z. Lu, The dynamic recrystallization evolution and kinetics of Ni–18.3Cr–6.4Co–5.9W–4Mo–2.19Al–1.16Ti superalloy during hot deformation, *J. Mater. Res.* 30 (2015) 1029–1041.
- [11] G.Z. Quan, D.S. Wu, G.C. Luo, Y.F. Xia, J. Zhou, Q. Liu, et al., Dynamic recrystallization kinetics in α phase of as-cast Ti–6Al–2Zr–1Mo–1V alloy during compression at different temperatures and strain rates, *Mater. Sci. Eng. A* 589 (2014) 23–33.
- [12] L. Cheng, H. Chang, B. Tang, H.C. Kou, J.S. Li, Deformation and dynamic recrystallization behavior of a high Nb containing TiAl alloy, *J. Alloys Compd.* 552 (2013) 363–369.
- [13] L. Suarez, P. Rodriguez-Calvillo, J.M. Cabrera, A. Martinez-Romay, D. Majuelos-Malloguin, A. Coma, Hot working analysis of a CuZn40Pb2 brass on the monophasic (β) and intercritical ($\alpha + \beta$) regions, *Mater. Sci. Eng. A* 627 (2015) 42–50.
- [14] B.J. Lv, J. Peng, Y.J. Wang, X.Q. An, L.P. Zhong, A.T. Tang, et al., Dynamic recrystallization behavior and hot workability of Mg–2.0Zn–0.3Zr–0.9Y alloy by using hot compression test, *Mater. Des.* 53 (2014) 357–365.
- [15] X.Y. Yang, Y. Okabe, H. Miura, T. Sakai, Effect of prior strain on continuous recrystallization in AZ31 magnesium alloy after hot deformation, *Mater. Sci. Eng. A* 535 (2012) 209–215.
- [16] D. He, J.C. Zhu, Z.H. Lai, Y. Liu, X.W. Yang, An experimental study of deformation mechanism and microstructure evolution during hot deformation of Ti–6Al–2Zr–1Mo–1V alloy, *Mater. Des.* 46 (2013) 38–48.
- [17] Y.C. Lin, J. Deng, Y.Q. Jiang, D.X. Wen, G. Liu, Hot tensile deformation behaviors and fracture characteristics of a typical Ni-based superalloy, *Mater. Des.* 55 (2014) 949–957.
- [18] L. Sun, K. Muszka, B.P. Wynne, E.J. Palmiere, On the interactions between strain path reversal and dynamic recrystallization in 316L stainless steel studied by hot torsion, *Mater. Sci. Eng. A* 568 (2013) 160–170.
- [19] M. Shaban, B. Eghbali, Determination of critical conditions for dynamic recrystallization of a microalloyed steel, *Mater. Sci. Eng. A* 527 (2010) 4320–4325.
- [20] T.C. Xu, X.D. Peng, J. Qin, Y.F. Chen, Y. Yang, G.B. Wei, Dynamic recrystallization behavior of Mg–Li–Al–Nd duplex alloy during hot compression, *J. Alloys Compd.* 639 (2015) 79–88.
- [21] H. Zhong, L.P. Feng, P.Y. Liu, T.T. Zhou, Design of a Mg–Li–Al–Zn alloy by means of CALPHAD approach, *J. Computer-Aided Mater. Des.* 10 (2003) 191–199.
- [22] C.L. Cui, L.B. Wu, R.Z. Wu, J.H. Zhang, M.L. Zhang, Influence of yttrium on microstructure and mechanical properties of as-cast Mg–5Li–3Al–2Zn alloy, *J. Alloys Compd.* 509 (2011) 9045–9049.
- [23] A.B. Ma, Y. Nishida, N. Saito, I. Shigematsu, S.W. Lim, Movement of alloying elements in Mg–8.5wt.%Li and AZ91 alloys during tensile tests for superplasticity, *Mater. Sci. Technol.* 19 (2003) 1642–1647.
- [24] A. Nayeb-Hashemi, J.B. Clark, A.D. Pelton, The Li–Mg (lithium–magnesium) system, *Bull. Alloy Phase Diagr.* 5 (1984) 365–374.
- [25] C.M. Sellars, W.J. Tegart, On the mechanism of hot deformation, *Acta Metall.* 14 (1966) 1136–1138.
- [26] X.S. Xia, Q. Chen, K. Zhang, Z.D. Zhao, M.L. Ma, X.G. Li, et al., Hot deformation behavior and processing map of coarse-grained Mg–Gd–Y–Nd–Zr alloy, *Mater. Sci. Eng. A* 587 (2013) 283–290.
- [27] X.S. Xia, Q. Chen, S.H. Huang, J. Lin, C.K. Hu, Z.D. Zhao, Hot deformation behavior of extruded Mg–Zn–Y–Zr alloy, *J. Alloys Compd.* 644 (2015) 308–316.
- [28] N. Tahrean, D.F. Zhang, F.S. Pan, X.Q. Jiang, D.Y. Li, D.L. Chen, Hot deformation and processing map of an as-extruded Mg–Zn–Mn–Y alloy containing I and W phases, *Mater. Des.* 87 (2015) 245–255.
- [29] E.I. Poliak, J.J. Jonas, A one-parameter approach to determining the critical conditions for the initiation of dynamic recrystallization, *Acta Mater.* 44 (1996) 127–136.
- [30] J.J. Jonas, X. Quenec, L. Jiang, E. Martin, The Avrami kinetics of dynamic recrystallization, *Acta Mater.* 57 (2009) 2748–2756.
- [31] H. Mirzadeh, A. Najafizadeh, Prediction of the critical conditions for initiation of dynamic recrystallization, *Mater. Des.* 31 (2010) 1174–1179.
- [32] B.J. Lv, J. Peng, L.L. Zhu, Y.J. Wang, A.T. Tang, The effect of 14H LPSO phase on dynamic recrystallization behavior and hot workability of Mg–2.0Zn–0.3Zr–5.8Y alloy, *Mater. Sci. Eng. A* 599 (2014) 150–159.
- [33] J.C.M. Hwang, R.W. Balluffi, On a possible temperature dependence of the activation energy for grain boundary diffusion in metals, *Scr. Metall.* 12 (1978) 709–714.
- [34] H.J. Frost, M.F. Ashby, *Deformation Mechanism Maps*, Pergamon Press, Oxford, 1982.
- [35] T.G. Langdon, Seventy-five years of superplasticity: historic developments and new opportunities, *J. Mater. Sci.* 44 (2009) 5998–6010.
- [36] H. Somekawa, T. Mukai, Effect of dominant diffusion process on cavitation behavior in superplastic Mg–Al–Zn alloy, *Scr. Mater.* 57 (2007) 1008–1011.
- [37] H.Q. Liang, H.Z. Guo, Y. Nan, C. Qin, X.N. Peng, J.L. Zhang, The construction of constitutive model and identification of dynamic softening mechanism of high-temperature deformation of Ti–5Al–5Mo–5V–1Cr–1Fe alloy, *Mater. Sci. Eng. A* 615 (2014) 42–50.
- [38] S. Mandal, M. Jayalakshmi, A.K. Buaduri, V.S. Sarma, Effect of strain rate on the dynamic recrystallization behavior in a nitrogen-enhanced 316L (N), *Metall. Mater. Trans. A* 45 (2014) 5645–5656.
- [39] S. Ni, Y.B. Wang, X.Z. Liao, S.N. Alhajeri, H.Q. Li, Y.H. Zhao, et al., Strain hardening and softening in a nanocrystalline Ni–Fe alloy induced by severe plastic deformation, *Mater. Sci. Eng. A* 528 (2011) 3398–3403.
- [40] S. Ni, Y.B. Wang, X.Z. Liao, S.N. Alhajeri, H.Q. Li, Y.H. Zhao, et al., Grain growth and dislocation density evolution in a nanocrystalline Ni–Fe alloy induced by high-pressure torsion, *Scr. Mater.* 64 (2011) 327–330.

- [41] T.G. Langdon, F.A. Mohamed, A new type of deformation mechanism map for high-temperature creep, *Mater. Sci. Eng.* 32 (1978) 103–112.
- [42] H. Watanabe, T. Mukai, K. Higashi, Deformation mechanism of fine-grained superplasticity in metallic materials expected from the phenomenological constitutive equation, *Mater. Trans.* 45 (2004) 2497–2502.
- [43] D.L. Ouyang, M.W. Fu, S.Q. Lu, Study on the dynamic recrystallization behavior of Ti-alloy Ti–10V–2Fe–3V in β processing via experiment and simulation, *Mater. Sci. Eng. A* 619 (2014) 26–34.
- [44] F.J. Humphreys, M. Hatherly, *Recrystallization and Related Annealing Phenomena*, second ed. Elsevier, Oxford, 2004.
- [45] B. Derby, The dependence of grain size on stress during dynamic recrystallisation, *Acta Metall.* 39 (1991) 955–962.
- [46] A.H. Chokshi, Cavity nucleation and growth in superplasticity, *Mater. Sci. Eng. A* 410–411 (2005) 95–99.